Accepted Manuscript

A closure model for predicting crack growth under creep-fatigue loading

Gabriel P. Potirniche

PII: S0142-1123(19)30111-2
DOI: https://doi.org/10.1016/j.ijfatigue.2019.03.029
Reference: JIJF 5044

To appear in: *International Journal of Fatigue*

Received Date: 15 December 2018
Revised Date: 5 March 2019
Accepted Date: 19 March 2019

Please cite this article as: Potirniche, G.P., A closure model for predicting crack growth under creep-fatigue loading, *International Journal of Fatigue* (2019), doi: https://doi.org/10.1016/j.ijfatigue.2019.03.029

A closure model for predicting crack growth under creep-fatigue loading

Gabriel P. Potirniche

Mechanical Engineering Department, University of Idaho, 875 Perimeter Drive MS 0902, Moscow, ID, 83844-0902, USA, email: gabrielp@uidaho.edu

ABSTRACT

A strip-yield model was formulated to simulate creep-fatigue crack growth and to quantify the influence of hold time on plasticity-induced crack closure during creep-fatigue crack growth. Creep-fatigue experiments have shown that longer creep hold times result in faster crack growth rates in subsequent fatigue cycles. This model advances the idea that a decrease of plasticity-induced crack closure is experienced by the crack during fatigue loading when a longer hold time is applied each creep-fatigue cycle. Consequently, the crack tip experiences an increase in the effective stress intensity factor range causing faster growth rate during the fatigue loading. The weight function method was used to compute stress intensity factors and surface displacements for cracks embedded in a material experiencing elastic, plastic and creep deformations at elevated temperatures. It is shown that the longer the hold time, the larger the creep deformation and crack opening displacements in the near crack-tip region. In turn, this leads to a decrease in the crack-tip opening stress/load and faster crack growth rates during the subsequent fatigue cycle. The model was used to perform simulations of creep-fatigue crack growth at elevated temperatures in a nickel-base superalloy and AISI 316 austenitic steel.

Keywords: *creep fatigue, plasticity-induced crack closure, strip yield model, nickel base alloy, austenitic 316 steel*

1. Introduction

Failure of structural components by creep-fatigue crack growth occurs when mechanical loading and elevated temperature act concurrently, conditions that are common in power plants, chemical plants and the aerospace industry. Numerous studies have been performed on creep-fatigue crack growth at elevated temperatures. However, understanding the mechanics of crack growth and predicting the measured rates of crack growth during creep-

fatigue loading is still an outstanding issue. The most common approach to compute creep-fatigue crack growth rates is to consider the linear summation of the crack growth rates during the fatigue and creep portions of each loading cycle. Oftentimes, models that use this additive rule disregard the interaction effects of the two loading modes. A limited number of models considered this interaction, for instance by adding an extra term to the sum, or by analyzing the crack-tip damage in front of the crack. The load interaction effect on creep-fatigue crack growth implies that the total crack growth rate is greater than the sum of the rates that a crack would experience under only creep or fatigue loading.

Fatigue crack growth in metallic alloys has been comprehensively studied over many decades. For constant amplitude fatigue loading, the Paris-Erdogan power law [1] using the stress intensity factor range ΔK as the input variable is able to predict the crack growth rates for long cracks in metals. To explain the load ratio effect on fatigue crack growth, Elber [2] proposed the concept of effective stress intensity factor ΔK_{eff}, which replaced ΔK in the Paris-Erdogan law and can explain crack acceleration and deceleration during variable amplitude loading. ΔK_{eff} values were computed by quantifying the plasticity-induced crack closure through the concept of crack-tip opening stress (S_{op}).

The influence of creep loading on S_{op} is a topic that has been almost entirely overlooked by the creep-fatigue community. The only previously published research on this topic was found to be that of Sehitoglu and Sun [3]. They employed two-dimensional finite element simulations to study the effect of load hold time on S_{op} in a cracked plate subjected to uniform tension loading. Sehitoglu and Sun showed that increasing hold time leads to larger *COD* and lower S_{op} values. Most recently, J. Ramirez et al. [4] performed a systematic study of the effect of hold time on S_{op} using two-dimensional and three-dimensional finite element simulations.

A computational approach that has been used effectively to characterize the plasticity-induced crack closure is strip-yield modeling. This technique has its source in the theoretical developments of Dugdale [5] and Barenblatt [6], who used a superposition of two elastic solutions to solve the problem of a crack embedded in an elastic-plastic region. Their approach was implemented in several computational models to simulate growing fatigue cracks. These computational strip-yield models have been used successfully to compute crack-tip opening stresses S_{op} caused by plasticity-induced crack closure under constant or variable amplitude loading. One of the first strip-yield models was that of Newman [7]. A main feature of the Newman model was that in order to deal with various test specimens, he used an equivalent center-crack simulation specimen and the *K*-equivalency principle for the computation of *K* and

COD in other specimen types. Using Newman's modeling framework, other strip-yield models have been proposed for fatigue crack growth. Nowadays, the standard methodology involves using integrals of weight functions instead of the *K*-equivalency principle to compute *K* and *COD* values for different specimens. Strip-yield models have been developed for fatigue crack growth [8-11], thermomechanical fatigue crack growth [12] and creep crack growth [13]. To date, there are no strip-yield models developed for creep-fatigue crack growth.

In this paper, a Strip-Yield Model for Creep-Fatigue Crack Growth (SYM-CFCG) was developed using the weight function method. Creep-fatigue crack growth rates were computed by summing the growth rates during the creep and fatigue portions of each loading cycle. The loading interaction effects on crack growth rates were accounted for by modeling the decrease of S_{op} with longer hold times. A key feature of this model is the computation of S_{op} values for cracked specimens loaded with creep-fatigue loading. The geometries analyzed were the middle-tension test (MT), single-edge notch test (SENT), double-edge notch tension (DENT) and compact-tension test (CT) specimens. SYM-CFCG was used to compute crack growth rates in a nickel-base superalloy and austenitic 316 stainless steel.

2. Mechanics of crack opening/closing during creep-fatigue loading

A typical creep-fatigue load cycle is illustrated in Fig. 1. The loading segments *A*-*B* and *C*-*D* represent the fatigue or cyclic portion of the cycle, and *B*-*C* the creep or hold time. The total crack growth during *A*-*D* is the sum of the crack growth during *A*-*B* and *B*-*C*. The main assertion of this study is that the hold time t_H during *B*-*C* affects the crack growth increment in the subsequent fatigue cycle, i.e., during *D*-*E*. This effect is a contributor to the commonly known load interaction effect on crack growth during creep-fatigue loading. For instance, this effect was observed and described in the case of creep-fatigue crack growth in a nickel-base superalloy by Piard et al. [14].

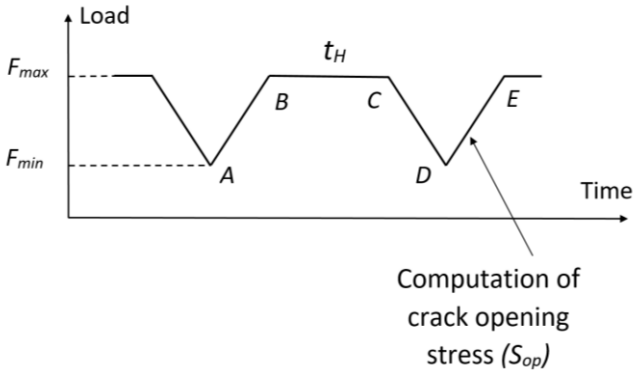

Fig. 1. A typical creep-fatigue load cycle used in laboratory crack growth testing.

The explanation that is proposed herein for the influence of hold time t_H on fatigue crack growth in the subsequent cycle relies on the concept of plasticity-induced crack closure and the mechanics of crack opening/closing during cyclic loading. Fig. 2 illustrates a qualitative description of the opening and closing of the crack surfaces at different points in the creep-fatigue cycle. At point B in the creep-fatigue cycle, the crack is loaded under the maximum stress. Therefore, the crack surfaces undergo a certain amount of crack opening *COD*.

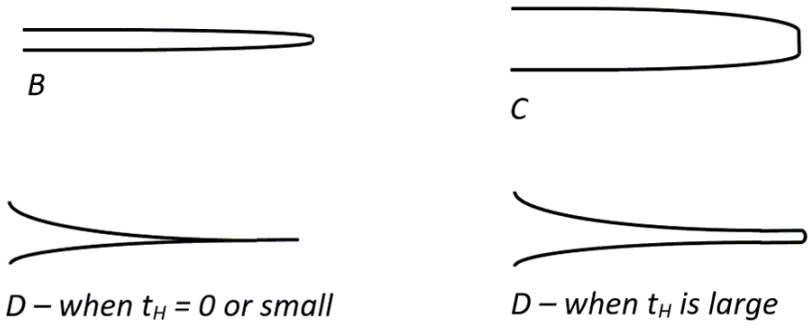

Fig. 2. Profiles of crack opening/closing displacements during a creep-fatigue cycle.

As a result of the accumulated creep strains at the end of t_H, at point *C* in the cycle, the *COD* further increases compared to its value at point *B*. The amount of this additional increase in *COD* is proportional to t_H. Upon unloading, the crack surfaces may end up partially or totally closed depending on the magnitude of t_H. When t_H is zero (fatigue loading) or small, the crack surfaces will be at least partially closed at minimum applied load (point *D* in the cycle). When t_H is big enough, the large *COD* induced during the hold time will prevent the crack from completely (or partially) closing at minimum load. In effect, for large enough values of t_H, the crack starts the new fatigue cycle *D-E* fully open. In this case, the effect of plasticity-induced crack closure is nullified by the additional *COD* acquired by the crack during the hold time. In turn, this leads to a drop in the opening stress to $S_{op} = S_{min}$ and maximizes the crack tip driving force during the fatigue cycle, i.e., $\Delta K_{eff} = \Delta K$. This phenomenon is expressed as

$$\left(\frac{da}{dN}\right)_{D-E} = f_1\left(S_{op},...\right), \text{ and } \left(S_{op}\right)_{D-E} \propto 1/t_H \tag{1}$$

The above considerations are supported by the previous finite element simulation results in [3-4]. Further experimental studies are needed to establish a quantitative relationship between S_{op} and t_H.

3. Strip-yield modeling of creep-fatigue crack growth

3.1. Modified Dugdale-Barenblatt model for plasticity and creep at the crack tip

Considering a cracked specimen subjected to mechanical loads at elevated temperatures, under cyclic and steady loads (Fig. 1), the material around the crack tip will experience instantaneous plastic strains and creep strains that accumulate over hold time t_H. A schematic of the plastic and creep zones at the crack tip is illustrated in the first picture of Fig. 3 for a cracked component subjected to a remote stress S.

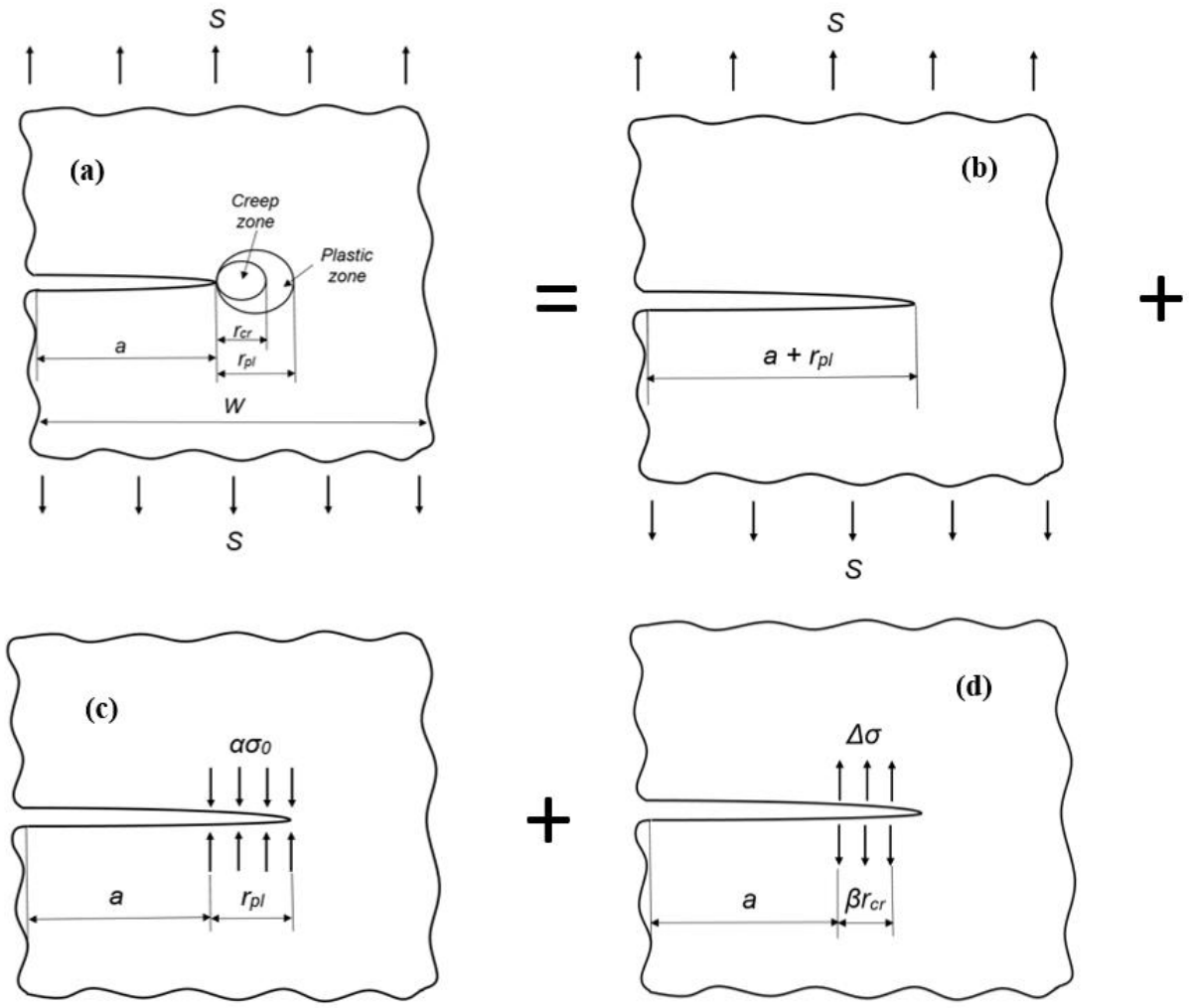

Fig. 3. Plastic and creep deformations at the crack tip, and the superposition principle applied to three elastic loading cases.

The crack problem illustrated in first schematic of Fig. 3 is replaced by a superposition of three simplified loading cases of the cracked component undergoing elastic deformations. First, the physical crack of length a is replaced by a fictitious crack of length $d = a + r_{pl}$, where r_{pl} is the plastic zone size at the physical crack tip. Second, the combination of remotely applied load, plasticity and creep zones at the crack tip is replaced by the linear

superposition of three elastic cases. These cases consider the elastic specimen with fictitious crack length d loaded as follows: *(i)* the remotely applied load S, *(ii)* a compressive segment load acting in the plastic zone equal to the flow stress $\alpha\sigma_0 = \alpha(S_y + S_{ut})/2$, and *(iii)* a tensile segment load $\Delta\sigma$, on the crack plane representing the stress relaxation due to creep strain accumulation. Here, α *is* the constraint factor (α =1 for plane stress, and α =3 for plane strain), S_y the yield strength and S_{ut} the ultimate strength of the material. The compressive segment load is applied on the entire plastic zone, while the tensile segment load is applied only on the corrected creep zone size by the factor β. If t_h is long enough causing the corrected creep zone to exceed the plastic zone, the application of $\Delta\sigma$ is then limited to the extent of the plastic zone, i.e., the corrected creep zone cannot exceed the plastic zone size.

3.2. Crack-tip plastic zone size

The plastic zone size r_{pl} is computed from the condition that the stress intensity factor at the tip of the fictitious crack with length $d = a + r_{pl}$ is zero,

$$K_{IS} + K_{I\sigma_0} = 0, \tag{2}$$

where K_{IS} is the stress intensity factor created by the remote loading S, and $K_{I\sigma_0}$ is the stress intensity factor due to the flow stress σ_0 in the plastic zone. Plastic zone size r_{pl} is computed by solving Eq. (2). The stress intensity factors are computed using the weight function method and the following formula

$$K_I = f\, S\sqrt{\pi d}\,, \tag{3}$$

where f is a non-dimensional geometrical factor that depends on the specimen type and geometry. Appendix A presents the formulas for f, K_{IS} and $K_{I\sigma_0}$ for two of the specimen types used in this study. Eq. (2) was solved for r_{pl} using the bisection method, and the integrals in K_{IS} and $K_{I\sigma_0}$ were computed using the 10-point Gauss quadrature.

3.3. Crack-tip creep zone size and stress relaxation during creep hold time

While the plastic zone computed in Section 3.2 develops instantaneously as the material yields under the applied load, the creep zone at the crack tip initiates and grows steadily during the hold time. The size of the crack-tip creep zone was computed using the formula introduced by Riedel and Rice [15]

$$r_{cr}(\theta,t)=\frac{1}{2\pi}\left(\frac{K_I}{E}\right)^2\left[\frac{(n+1)^2 E^n B t}{2n\alpha_n^{n+1}}\right]^{\frac{2}{n-1}} F_{cr}(\theta), \tag{4}$$

where K_I is mode I stress intensity factor, n and B are the stress exponent and coefficient in Norton creep law, respectively, θ is angle and t is time. The parameter $F_{cr}(\theta)$ was considered for $\theta = 90°$, and its values as a function of n for the plane stress and plane strain cases were given by Riedel and Rice, and are presented in Table 2. The variable α_n is calculated as

$$\alpha_n=\left(\frac{n+1}{n}\frac{\pi}{I_n}\right)^{\frac{1}{n+1}} \quad \text{for plane stress,}$$

$$\alpha_n=\left[\frac{n+1}{n}\frac{\pi(1-\upsilon^2)}{I_n}\right]^{\frac{1}{n+1}} \quad \text{for plane strain.} \tag{5}$$

The value of I_n was given by Hutchinson [16], and is presented in Table 1. When n had a value other than those shown in Table 1, linear interpolation was performed to obtain I_n.

Table 1. I_n factor for the computation of the creep zone size [16].

I_n				
n	3	5	9	13
Plane stress	3.86	3.41	3.03	2.87
Plane strain	5.51	5.01	4.60	4.40

Table 2. F_{cr} factor for the computation of the creep zone size [15].

$F_{cr}(\theta=90°)$			
n	3	5	13
Plane stress	0.25	0.32	0.38
Plane strain	0.55	0.5	0.3

Creep deformation causes stress relaxation in the near crack tip region. According to an equation introduced by Riedel [17], the stress components relax proportionally to $(1/t)^{1/(n+1)}$. The Riedel formula cannot be directly applied directly, as it refers to the stress tensor components in the multiaxial stress state at the crack tip. For the uniaxial stress case of the strip yield model, the variation of the segment stress in the creep zone was taken as

$$\Delta\sigma = \sigma_0 \left[1 - \left(\frac{t_0}{t} \right)^{\frac{1}{n+1}} \right], \tag{6}$$

where t is time, t_0 is a time constant taken as $t_0 = 10^{-3}$ hours (3.6 seconds) for all simulations in this study. This equation preserves the Riedel format of flow stress relaxation, and no creep strains accumulate if $t_H \leq 3.6$s.

The actual stress relaxation is considered to occur not only within the creep zone of size r_{cr}, but also over an extended region ahead of the crack tip, i.e., the corrected creep zone size, which is computed as βr_{cr}. For all simulations in this study, the correction factor β was chosen as 3.5 for the nickel-base superalloy, and 3.0 for the 316 stainless steel. When the corrected creep zone reached and exceeded the size of the plastic zone, it was limited to the size of plastic zone. Therefore, a limited impact of the correction factor is considered in this model. The correction factor β for the creep zone size was chosen from parametric studies that identified the value that best fits the resulting creep-fatigue crack growth rates for the loading waveform with the smallest considered hold time. Then, this value was kept constant for all other creep-fatigue simulations with different hold times.

3.4. Meshing of the crack plane and crack advance

The superposition approach illustrated in Fig. 3 is implemented using the strip-yield modeling framework introduced by Newman [7]. Prior to the onset of crack growth, the crack plane, including both the crack surface and plastic zone, is meshed using 15 one-dimensional elements, of which 10 are assigned to the plastic zone ahead of the physical crack tip and 5 to the cracked surface behind the crack tip. These elements exhibit an elastic-plastic-creep behavior, experiencing stress and elongation during each loading cycle. Fig. 4 shows the elements in the crack plane mesh. Each element i has a given width w_i and length (L_i). The initial element widths w_i in the crack-tip plastic zone and crack surface behind the crack tip are given in Table 3.

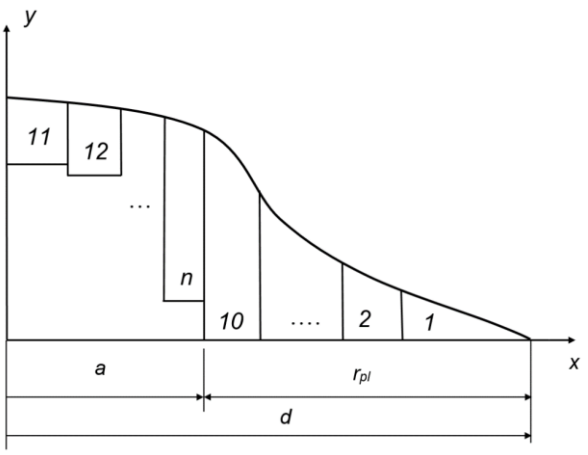

Fig. 4. Crack-plane mesh.

The crack plane mesh changes during crack advance by two processes, namely the element creation and element deletion by lumping. After the plastic zone size r_{pl} is calculated at maximum load in the creep-fatigue cycle, the physical crack length a is increased by a fraction ρ of the plastic zone size, ρr_{pl}. In this study, $\rho = 0.05$ was chosen for all simulations, which is the same as the value used by Newman [7]. Simulations were also performed with different ρ values, and they indicated that $\rho = 0.05$ is the optimum fraction of the plastic zone for the crack growth increment to produce similar results with established literature data on opening stresses for fatigue crack growth. After the crack length is increased by the crack growth increment, $a = a + \rho r_{pl}$, the plastic zone size is recalculated and re-meshed using the element widths presented in the Table 3. As the crack tip advances, element 10, which used to be part of the plastic zone mesh, becomes a part of the crack surface behind the crack tip.

Table 3. Element widths for the initial mesh of the crack plane. w_i is the element width, and r_{pl} is the plastic zone size.

Element #	**Normalized element size in the plastic zone** $\left(w_i/r_{pl}\right)$	**Normalized element size in the cracked surface** $w_i/\left(r_{pl}a_i\right)$
1	0.3	0.3
2	0.2	0.2
3	0.15	0.15
4	0.12	0.12
5	0.09	0.09
6	0.06	–
7	0.04	–
8	0.02	–
9	0.01	–
10	0.01	–

With each loading cycle, the number of elements in the crack surface mesh increases, because new elements are added to it. To preserve computational efficiency, element lumping in the crack surface mesh occurs whenever the total number of elements in the crack plane, including the plastic zone and crack surface, exceeds a prescribed value, which for all studies was set at 35 elements, which is the same range as the number of elements (20-30) used by Newman [7]. Whenever lumping occurs, elements 11 and 12, which are located the farthest from the crack tip, are lumped into one element, so that the new element 11 will have the following coordinate, width, length and stress, respectively

$$x_{11} = \frac{x_{12} + \frac{w_{12}}{2}}{2}\ ,\ w_{11} = w_{11} + w_{12}\ ,\ L_{11} = \frac{L_{11}w_{11} + L_{12}w_{12}}{w_{11} + w_{12}}\ ,\ \sigma_{11} = \frac{\sigma_{11}w_{11} + \sigma_{12}w_{12}}{w_{11} + w_{12}}\ . \tag{7}$$

3.5. Crack surface displacements and element lengths at maximum load in the cycle

Crack surface displacements are the result of two types of applied loads, i.e., the remote stresses at the boundaries of the specimen, and the segment loading applied in the crack plane. These applied loads are illustrated in Fig. 3. For the crack of length $d = a + r_{pl}$, the crack surface displacement in the vertical direction y at a point x on the crack plane is defined as $u(d,x)$. From Fig. 3, by superposition,

$$u\left(d,x\right) = u\left(d,x,S\right) + u\left(d,x,\sigma_0\right) + u\left(d,x,\Delta\sigma\right), \tag{8}$$

where, $u(d,x,S)$ is the crack surface displacement at location x caused by a remote stress S, while $u(d,x,\sigma_0)$ and $u(d,x,\Delta\sigma)$ are the crack surface displacements at x caused by the local segment loading σ_0 and $\Delta\sigma$, respectively. The displacements in the above equation are computed using the weight function method. According to Wu and Carlsson [18], the crack surface displacement in the normalized form at location x is given by

$$u\left(d,x,\sigma\right) = \frac{\sigma}{E'}\int_{a_0}^{d}\left[\ f\left(\xi\right)\sqrt{\pi\xi}\ \right]\cdot m\left(\xi,x\right)d\xi\ . \tag{9}$$

where $m(d,x)$ is the weight function for a crack of length d subjected to a stress σ. The Wu and Carlsson weight functions have different forms for the center-crack versus edge-crack specimens. For a center-crack specimen, the above equation is

$$u(d,x,\sigma)=\frac{\sigma}{E'}\int_{a_0}^{d} f(s)\sum_{i=1}^{I}\beta_i(s)\left[1-\left(\frac{x}{s}\right)^2\right]^{i-\frac{3}{2}} ds\,, \tag{10}$$

and for an edge crack specimen is

$$u(d,x,\sigma)=\frac{\sigma}{E'\sqrt{2}}\int_{a_0}^{d} f(\xi)\sum_{i=1}^{I}\beta_i(\xi)\left(1-\frac{x}{\xi}\right)^{i-\frac{3}{2}} d\xi\,, \tag{11}$$

where I is an index that depends on the specimen type. The lower integration limit a_0 is defined according to the loading mode of the crack. When the entire crack surface is loaded by a stress σ, e.g., the case of remotely applied loading, then $a_0 = x$. In the case of segment load σ on the crack surface between x_1 and x_2, the lower integration limit $a_0 = \max(x_1,x)$. The factors β_i are given in Appendix B, the crack surface displacements for remote loading in Appendix C, and those for segment loading in Appendices D and E.

Once the crack surface displacements u_i are computed at maximum load, the lengths for the plastic zone elements are set to these values, i.e., $L_i = u_i$ for $i = 1,2,\ldots,10$. In the first cycle of the creep-fatigue simulation, the lengths of the elements in the physical crack surface are all set to zero. For ulterior cycles, these lengths are the ones computed in the previous cycle, unless a new element 11 is created by crack extension and lumping. The length of the new element 11 resulting from the lumping process is given in Eq. (7).

3.6. Contact stresses and new element lengths at minimum load

Upon unloading, stresses are computed for the elements in the plastic zone and crack surface. At minimum load, the stress in each element j is computed by solving the following compatibility equation

$$u_i = L_i = u(d,x_i,S_{\min})+\sum_{j=1}^{n} u(d,x_i,x_j,\sigma_j), \tag{12}$$

where $u(d,x_i,S_{min})$ is the displacement created at element i by remotely applied stress S_{min} and $u(d,x_i, x_j,\sigma_j)$ is the displacement at element i created by a segment load σ_j applied at element j of coordinate x_j. This situation is illustrated in Fig. 5.

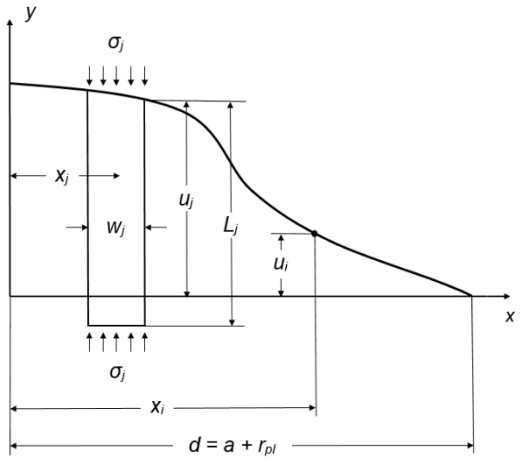

Fig. 5. Crack surface displacement at point *i* created by the stress in element *j*.

From the above equation, element stresses σ_j are computed using a Gauss-Seidel method with constraints, as described in [7]. These constraints are defined for the plastic zone and crack surface elements as follows. For the plastic zone elements, (a) if $\sigma_j \le -\sigma_0$, then $\sigma_j = -\sigma_0$, and (b) if $\sigma_j \ge \alpha\sigma_0$, then $\sigma_j = \alpha\sigma_0$. For the elements on the crack surface, (a) if $\sigma_j \ge 0$, then $\sigma_j = 0$, and (b) if $\sigma_j \le -\sigma_0$, then $\sigma_j = -\sigma_0$. After element stresses are calculated at minimum load, element lengths are recalculated for each of the elements that are yielded (tension or compression) at this point in the cycle. New lengths for yielded elements are computed according to the procedure described in Section 3.5 and using the new stress distribution computed at minimum load. This is done according to the following equation only for the elements for which $\sigma_i = -\sigma_0$ when $S = S_{min}$,

$$L_i = u\left(d, x_i\right) = u\left(d, x_i, S_{\min}\right) + \sum_{j=1}^{n} u\left(d, x_i, \sigma_j\left(x_j\right)\right). \tag{13}$$

3.7. Computation of crack-tip opening stresses

Crack-tip opening stress S_{op} (or load F_{op} in the case of compact tension specimens) is the key variable in this model because it determines the variation of the crack growth rates under creep-fatigue loading with various hold times. Two methods have been used in this study to compute S_{op}, namely, the stress intensity and the crack surface displacement methods.

The first method of computing the crack-tip opening stress requires that K_I from the application of the remote stress increment $\Delta S = S_{op} - S_{min}$ equals K_I created by the contact stresses on the crack surface at minimum load,

$$K_{I\left(S_{op} - S_{\min}\right)} + \sum_{j=11}^{n} K_{I\sigma_j} = 0, \tag{14}$$

where $K_{I\left(S_{op}-S_{\min}\right)}$ is the mode I stress intensity factor created on the physical crack length a by the stress increment $S_{op} - S_{min}$, and $K_{I\sigma_j}$ is the stress intensity created by the stress σ_j at element j on the crack surface (not including the plastic zone). This equation was solved for S_{op} using the bisection method.

The second method uses a condition on the crack surface displacements described by Daniewicz et al. [10]. Assuming the stress distribution in the crack surface elements at minimum load, the opening stress S_{op} is the remote stress that fully opens the crack at each element i on the crack surface. This condition is written as

$$u\left(a, x_i, S_{op} - S_{\min}\right) + \sum_{j=11}^{n} u\left(a, x_i, \sigma_j\left(x_j\right)\right) = 0 \cdot \tag{15}$$

S_{op} is computed from the above equation using the bisection method. The crack surface displacements u in the above equation caused by either remote loading $S_{op} - S_{min}$ or local segment loading σ_j are determined according to the formulas described in Appendices C, D and E.

Simulations were performed using the two methods for computing S_{op}, and similar results were obtained, with small discrepancies. The crack surface displacement method yielded the closest values to the previously published results on crack opening stresses for fatigue crack growth. Consequently, this method has been used throughout this study to produce predictions of S_{op} and estimate creep-fatigue crack growth rates.

3.8. Computation of crack growth rates

To compute crack growth rates, one calculates the number of cycles dN required to growth the crack by an increment da. The calculation of da was described in section 3.4. The crack growth rate per cycle during a creep-fatigue cycle is computed as

$$\left(\frac{da}{dN}\right) = \left(\frac{da}{dN}\right)_{fat} + \left(\frac{da}{dN}\right)_{cr}, \tag{16}$$

where $(da/dN)_{fat}$ is the fatigue crack growth rate per cycle during the increasing portion of the loading, and $(da/dN)_{cr}$ is the creep crack growth rate per cycle during the holding portion of the loading. The fatigue crack growth rate equation is

$$\left(\frac{da}{dN}\right)_{fat} = C \cdot \Delta K_{eff}^{m}, \tag{17}$$

where C and m are material constants, and $\Delta K_{eff} = K_{max} - K_{min}$ is the effective stress intensity factor range. The crack growth rate for creep is

$$\left(\frac{da}{dN}\right)_{cr} = C' \cdot K_{\max}^{m'} \cdot t_H \,, \tag{18}$$

where C' and m' are material constants, and t is time. Using these equations, the number of creep-fatigue cycles needed to grow the crack by da is

$$dN = \frac{da}{C \cdot \Delta K_{eff}^{m} + C' \cdot K_{\max}^{m'} \cdot t_H} \,. \tag{19}$$

4. Model verification

The model verification was performed by comparing predicted crack-tip opening stresses for fatigue crack growth with established results from other studies that used either the strip-yield or finite element modeling methods. The verification was performed for all specimen types, MT, SENT, DENT and CT. Plasticity-induced crack closure for fatigue crack growth has been thoroughly studied in the last several decades. It is well known that the crack-tip opening stress during fatigue crack growth increases from the minimum stress in the cycle at the onset of crack growth to some stabilized value during steady crack growth. The most important portion of the fatigue life from the standpoint of plasticity-induced crack closure is the steady crack growth when the crack-tip opening stress stabilizes or vary little from one cycle to another. The results included in this section include only stabilized values of the opening stresses, after a certain number of cycles. The results are presented for values of applied stresses to flow stress, thus they can be applied to any material of interest.

Fig. 6 presents a comparison of the opening stresses for the MT, SENT and DENT specimens, at load ratios of $R = -1$ and $R = 0$, and ratios of K_{max}/K_0 between 0.1 and 0.7. All simulations were performed in plane stress conditions. The initial crack length to specimen width ratio in all simulations was $a/W = 0.1$. The results from the SYM-CFCG model are compared with the results from finite element modeling by McClung [19] and strip-yield modeling by Newman [20]. In all cases, the agreement between the three models is good, with small discrepancies between the strip-yield models and the finite element model in the case or $R = -1$ for ratios of K_{max}/K_0 ranging from 0.2 to 0.45, however, the difference between these models is not significant.

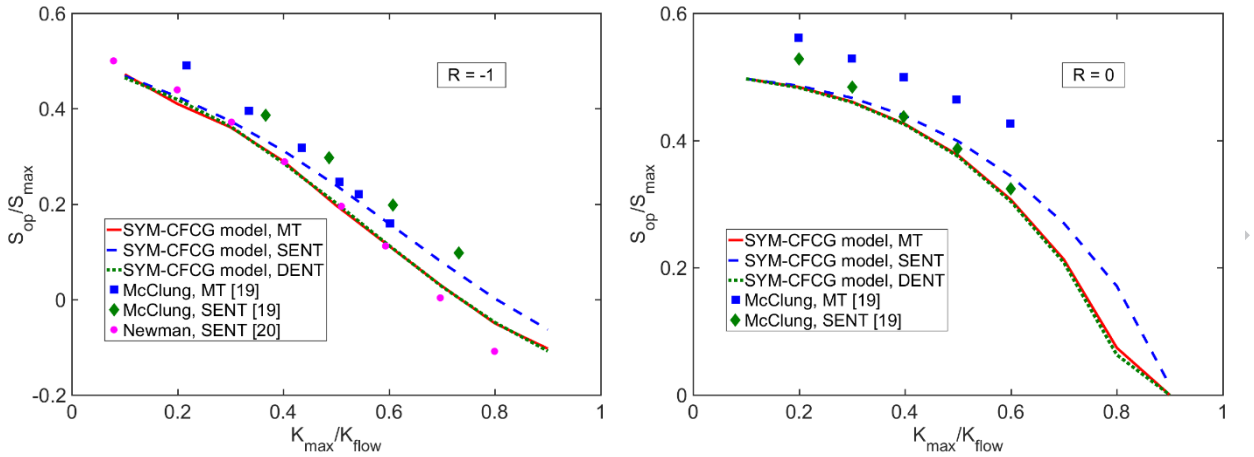

(a) **(b)**

Fig. 6. Comparison between the predictions of the SYM-CFCG model, strip-yield modeling [20] and finite element simulations [19] of crack-tip opening stresses for fatigue crack growth in the MT, SENT and DENT specimens, plane stress (α = 1) for two load ratios: (a) $R = -1$, and (b) $R = 0$.

The second verification was performed for the CT specimen. In this case, the SYM-CFCG model predictions are compared with those of the strip-yield modeling by Wang and Blom [9]. Fig. 7a shows the comparison of the predicted opening force normalized by the maximum applied force, P_{op}/P_{max}, for load ratios ranging from $R = -1$ to $R = 0.8$, and for three constraint factors, $\alpha = 1$ (plane stress), $\alpha = 2$ and $\alpha = 3$ (plane strain). Fig. 7b presents the comparison of the normalized opening force for three values of the applied maximum force in plane stress case. In this case, the maximum applied force in the fatigue cycle is normalized by the force that would cause the net flow stress σ_0 in the uncracked section of the specimen. In all cases, the agreement between the SYM-CFCG and the Wang and Blom models is satisfactory, with only slight differences for the load ratio of $R = -1$. Any difference in predicted S_{op} values between the two models is likely caused by the different weight functions used in each of them.

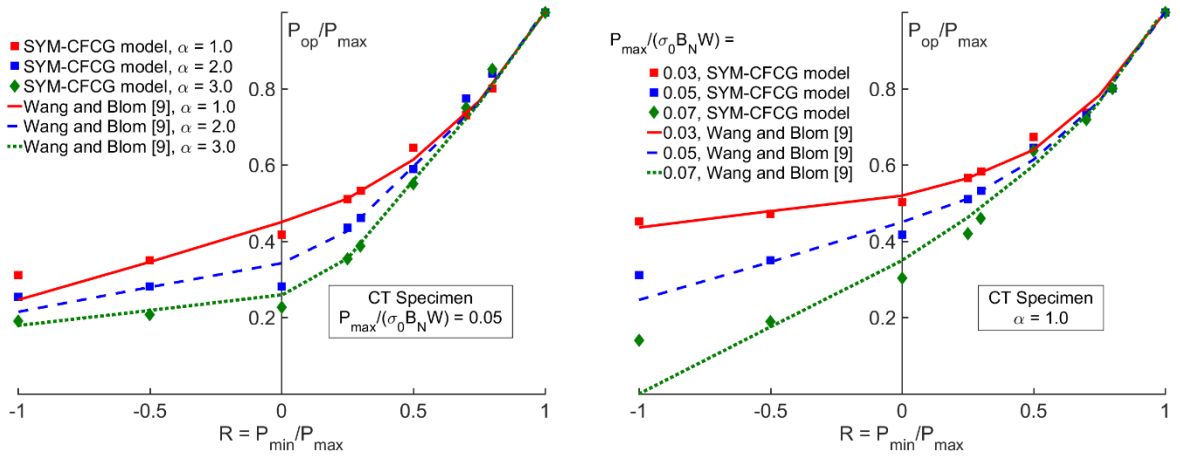

Fig. 7. Comparison between the predictions of the SYM-CFCG and strip-yield modeling [9] of crack tip opening stresses in CT specimens for: (a) three constraint factors, and (b) three values of maximum applied loads in plane stress. σ_0 is flow stress, B_N thickness and W width.

5. Results and discussion

This section presents SYM-CFCG model predictions of creep-fatigue crack growth in a nickel-base superalloy and 316 austenitic stainless steel. The experimental data used for comparison with the model predictions was taken from published studies. For each case, the material constants, specimen geometry and loading were the same in SYM-CFCG simulations as those in the respective published studies, whenever data were available. The material constants used for each material are indicated in Table 4. The elastic constants, yield and ultimate strengths, and the Norton creep law constants were obtained as described in Sections 5.1 and 5.2 for the nickel-base superalloy and 316 austenitic stainless steel, respectively. Coefficient C and exponent m in the fatigue crack growth law (Eq. (17)) were obtained by performing a parametric study to determine the effective crack growth rate curve (i.e., da/dn vs. ΔK_{eff}) that produced the best fit for the low R-ratio fatigue crack growth rate curve (i.e., da/dn vs. ΔK). The coefficient C' and exponent m' in the creep crack growth law (Eq. (17)), were obtained by a curve fit performed on the creep-fatigue test with the lowest hold time greater than zero. For all simulations using SYM-CFCG, the plane stress case (α = 1.0) was considered.

5.1. Powder metal nickel-base superalloy

Creep-fatigue crack growth simulations were performed in a powder metal nickel-base superalloy (Astroloy) used for gas turbine components, and the model results were compared with the experimental data published by Piard et al. [14]. Piard et al. performed a study to measure crack growth rates during creep-fatigue loading with hold time of 0, 30s, 300s and 1000s in Astroloy SENT specimens at 750°C. The particularly relevant aspect of the Piard et al. study is that they measured the total crack growth rate *da/dN* in each cycle, as well as the crack growth rates during the cyclic $(da/dN)_{fat}$ and holding $(da/dN)_{cr}$ portions of each cycle. Thus, they were able to clearly identify the dependence of the $(da/dN)_{fat}$ on the duration of hold time t_H. Piard et al. showed that the longer t_H, the faster the crack growth rate in the cyclic loading $(da/dN)_{fat}$, undoubtedly highlighting the load interaction effect on creep-fatigue crack growth.

Table 4. Material constants used in simulations.

Property	PM Astroloy	316 SS - annealed	316 SS - 20% cold worked
T (°C)	750	593	593
E (GPa)	160	153	153
v	0.3	0.32	0.32
S_y (MPa)	910	148	364
S_{ut} (MPa)	910	435	617
B ($h^{-1}MPa^{-n}$)	$1.01 \cdot 10^{-27}$	$6.35 \cdot 10^{-33}$	$2.79 \cdot 10^{-26}$
n	8.5	11.83	8.76
C	$6.48 \cdot 10^{-8}$	$1.6 \cdot 10^{-5}$	$3.0 \cdot 10^{-5}$
m	3.1	1.5	1.2
C'	$6.5 \cdot 10^{-8}$	$1.5 \cdot 10^{-7}$	$6.5 \cdot 10^{-4}$
m'	3.8	3.7	2.1
β	3.5	3.0	3.0
α	1.0	1.0	1.0

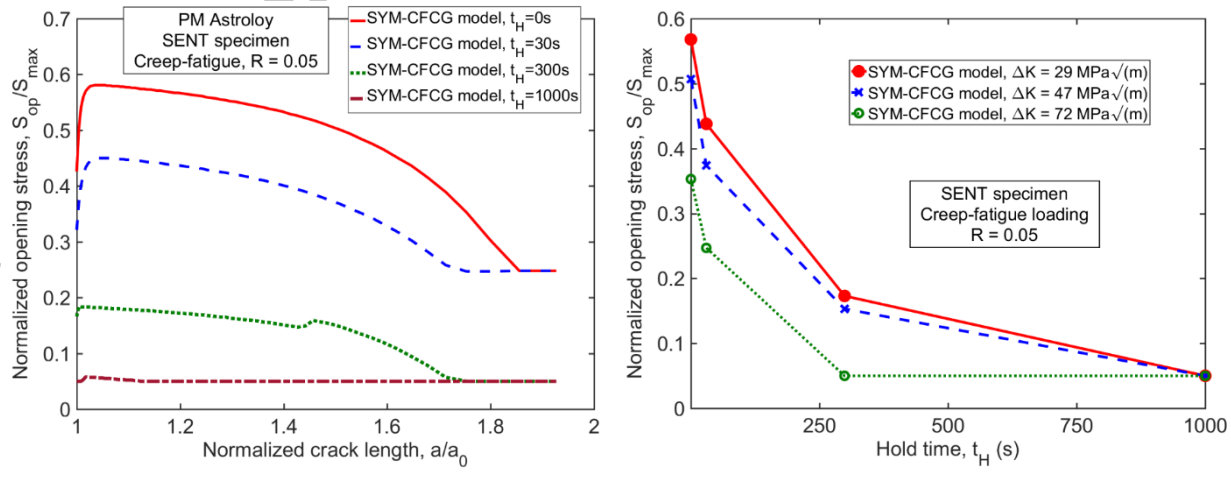

(a) **(b)**

Fig. 8. (a) Evolution of crack-tip opening stress with crack growth for fatigue and creep-fatigue loading with different hold times in a PM Astroloy material; (b) Variation of peak opening stress as a function of hold time at various stress intensity factor ranges ΔK during the crack growth history in a PM Astroloy material.

SYM-CFCG simulations of crack growth under creep-fatigue loading were performed for the specimen and loading conditions studied by Piard et al. Fig. 8a shows the evolution of the crack-tip opening stress for fatigue (t_H = 0s) and creep-fatigue with t_H = 30s, 300s and 1000s. In the case of fatigue crack growth, the expected evolution of the opening stress is obtained from the SYM-CFCG simulations, with the rapid initial increase of S_{op} due to plastic wake build-up behind the crack tip as the crack starts growing. Then, a relatively stabilized portion of the S_{op} is observed, followed by a rapid decrease in S_{op} as the crack approached the final failure region. The decreasing portion of the curve is due to the crack opening displacements increasing greatly with longer crack length and ΔK approaching the fracture toughness of the material. For most of the fatigue crack growth history, the opening stresses ranged between 0.58-0.5S_{max}. For creep-fatigue crack growth with the three different hold times, the opening stress S_{op} decreased throughout the entire history of crack growth. Fig. 8a shows that the longer the hold time, the lower the S_{op}. In the case of the largest simulated hold time of t_H = 1000s, the opening stress drops to the minimum stress, $S_{op} = S_{min} = 0.05S_{max}$, which means that the crack is always open during the creep-fatigue cycle, and the plasticity-induced crack closure is effectively canceled by the additional crack opening incurred during creep holding. In turn, decreasing S_{op} values with longer hold times leads to faster crack growth rates during the cyclic loading, $(da/dN)_{fat}$. The variation of the stabilized (maximum) opening stresses during crack growth with hold time is illustrated in Fig. 8b. These S_{op} values are reported for three ΔK levels corresponding to the initial phase of crack growth (ΔK = 29 MPa$\sqrt{m}$), the middle portion of the crack growth life (ΔK = 47 MPa$\sqrt{m}$), and the final stage of crack growth immediately before the final fracture (ΔK = 72 MPa$\sqrt{m}$). In all three ΔK cases, the opening stress decreases with hold time, eventually reaching minimum applied load in the cycle at the end of crack growth.

The effect of hold time on opening stresses illustrated in Fig. 8 can be understood if one analyzes the distribution of *COD* at maximum load and contact stress on the crack surfaces at minimum load. Fig. 9a shows the *COD* at maximum load in the cycle (point C in Fig. 1), after the application of the hold time and for the crack length that gives ΔK = 47 MPa$\sqrt{m}$. The fictitious crack tip of coordinate $d = a + r_{pl}$ is at a normalized position of x/d = 1, and the physical crack tip of coordinate a is at x/d = 0.96. For fatigue loading (t_H = 0s), the resulting *COD* is lower than that when the loading includes an additional hold time. The added *COD* is the result of flow stress relaxation and accumulation of creep deformation in the crack plane in front of the crack tip. It can also be observed that the

COD in the case of creep-fatigue loading with t_H = 1000s is almost twice as large as the one when only fatigue loading is applied.

An analysis of the results shown in Fig. 9b also enhances the understanding of the creep loading effect on crack-tip opening stresses. This figure shows the variation of the contact stresses between the crack surfaces at minimum load (point D in Fig. 1). It can be observed that the contact compressive stresses are most significant in the case of fatigue loading, and they diminish with the application of a longer hold time. When t_H = 1000s, the contact stresses behind the physical crack tip become zero, thus the plastic wake behind the crack tip loses completely its effectiveness in closing the crack at minimum load.

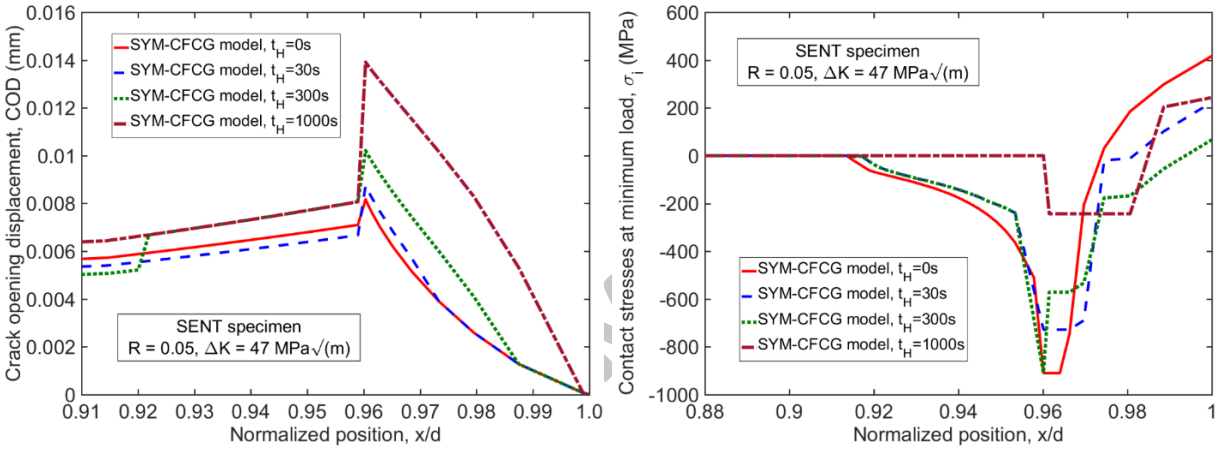

(a) **(b)**

Fig. 9. Variation in the near crack-tip region of: (a) crack opening displacements at maximum load, and (b) contact stresses between crack surfaces at minimum load. The physical crack length is at a = 26.93 mm (normalized position x/d = 0.96), and the fictitious crack tip is at $d = a + r_{pl}$ = 28.05 mm (normalized position x/d = 1.0).

Using the obtained opening stresses for creep-fatigue loading with different hold times, crack growth rates were computed for the fatigue portion of the cycle and for the total creep-fatigue cycle. Fig. 10a shows the predictions of $(da/dN)_{fat}$ from the SYM-CFCG model and the comparison with the experimental values of Piard et al. The SYM-CFCG model predicts well most of the data for the four considered hold times. There is some discrepancy between the experimental data and the SYM-CFCG values for the hold time of t_H = 1000s. This could be attributed to some additional damage mechanism at the crack tip that occurs during creep loading, which is not accounted for in this model. An interesting features is the initial drop in the $(da/dN)_{fat}$ curve, which is observed only for fatigue loading. The tendency of opening stresses to decrease in the initial phase of crack growth decreases with increasing hold

times. This phenomenon is observed in Fig. 10a in both the experimental data and SYM-CFCG model predictions, and it can be explained by the fact that initially the crack does not have a plastic wake, so the initial crack growth rate is high. As the crack tip advances through the initial crack-tip plastic zone, the crack surfaces develop a plastic wake, which slows down the crack growth rate by some amount. Once the plastic wake reaches a stable thickness, the crack growth rate accelerates again due to the increase in the stress intensity factor range because of crack length increase. While this behavior is particular for fatigue crack growth, in the case of creep-fatigue loading the influence of the plastic wake is diminished, or even eliminated at longer hold times, as a result of the accumulated creep strains and added *COD* during the hold time. Fig. 10b illustrates the total crack growth rate *da/dN*, which includes both the fatigue and creep growth rates as a function of ΔK. The plot presents a comparison between the experimental values and the SYM-CFCG predictions, and good agreement is observed for the four tests performed.

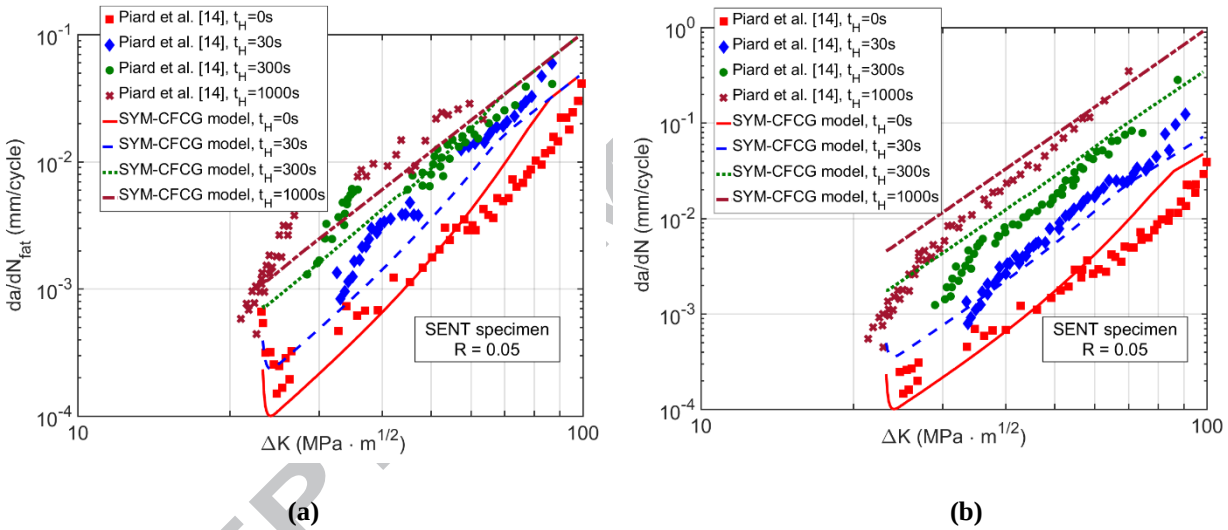

Fig. 10. Comparison between SYM-CFCG model predictions and experimental measurements of Piard et al. [14] during creep-fatigue loading for: (a) fatigue crack growth rates $(da/dN)_{fat}$, and (b) total crack growth rates *da/dN*.

The influence of creep hold time on crack-tip opening stresses produces a load frequency effect for a certain range of frequency values. The load frequency effect for the experiments of Piard et al. and the SYM-CFCG simulations is illustrated in Fig. 11. In this plot the crack growth rates for the creep $(da/dN)_{cr}$ and fatigue $(da/dN)_{fat}$ are plotted, along with their linear superposition by simply adding the two together. The $(da/dN)_{fat}$ line is computed by the SYM-CFCG model from the fatigue crack growth simulation, when t_H = 0s, thus, it does not depend on frequency. The $(da/dN)_{cr}$ line is the creep crack growth law given in Eq. (18). The dotted line in Fig. 11 is the linear superposition of the two crack growth equations, i.e. for $(da/dN)_{fat}$ and $(da/dN)_{cr}$. The SYM-CFCG predictions are

also shown in this figure, and one can observe that these predictions are situated consistently higher that the linear summation (dotted) line, which clearly indicates a load frequency effect on the total crack growth rate *da*/*dN* that is captured by the SYM-CFCG model. The most relevant difference is observed for the frequency of f = 0.033 Hz (t_H = 30s). The load frequency effect is less relevant when f = 0.0033 Hz (t_H = 300s) or f = 0.001 Hz (t_H = 1000s), and totally inexistent when f = 10 Hz (t_H = 0s). This can be explained considering that for f = 0.0033 Hz and f = 0.001 Hz creep crack growth is dominant, while for f = 10 Hz fatigue crack growth is the only loading mode. On the same plot, the Piard et al. data are also plotted, and while their data show a strong frequency effect at f = 0.033 Hz, the effect is not visible for other frequencies. This is due mainly to the variability in the experimental data of *da*/*dN* versus ΔK at the considered value of ΔK = 47 MPa√m, but the frequency effect is relevant from their experiments as well, if one considers the data in Fig. 10a.

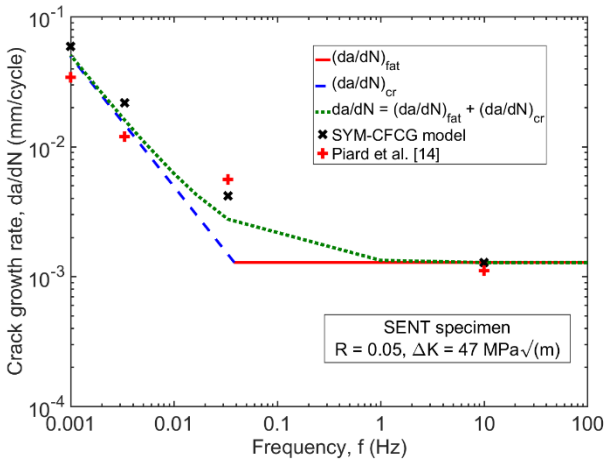

Fig. 11. Load interaction effect on creep-fatigue crack growth rates for a PM Astroloy material.

5.2 AISI 316 austenitic stainless steel

Creep-fatigue crack growth in AISI 316 stainless steel was performed by Michel and Smith [21] in SENT specimens and Sadananda and Shahinian [22] in CT specimens at a temperature of T = 593°C, with the material in the annealed and 20% cold worked conditions. The material constants for the 316 stainless steel in the two conditions are presented in Table 4. The Young's modulus E values were taken from the British Stainless Steel Association website [23], the yield and ultimate strengths from the American Iron and Steel Institute website [24] and the AKSteel data product bulletin [25], while the Norton creep constants from Monterio et al. [26] study.

Figs. 12a and 12b show the evolution of the normalized opening stress/force during creep-fatigue crack growth in the annealed SENT specimens and the 20% cold worked SENT and CT specimens, respectively. At both temperatures, the applied load ratio was R = 0 and the hold times were t_h = 0s, 6s and 60s. It can be observed that the opening stress decreases with increasing hold time. The difference in the opening stress curves for t_h = 0s and t_h = 6s is small, however, a significant decrease in the opening stress is recorded when the hold time is increased to t_h = 60s.

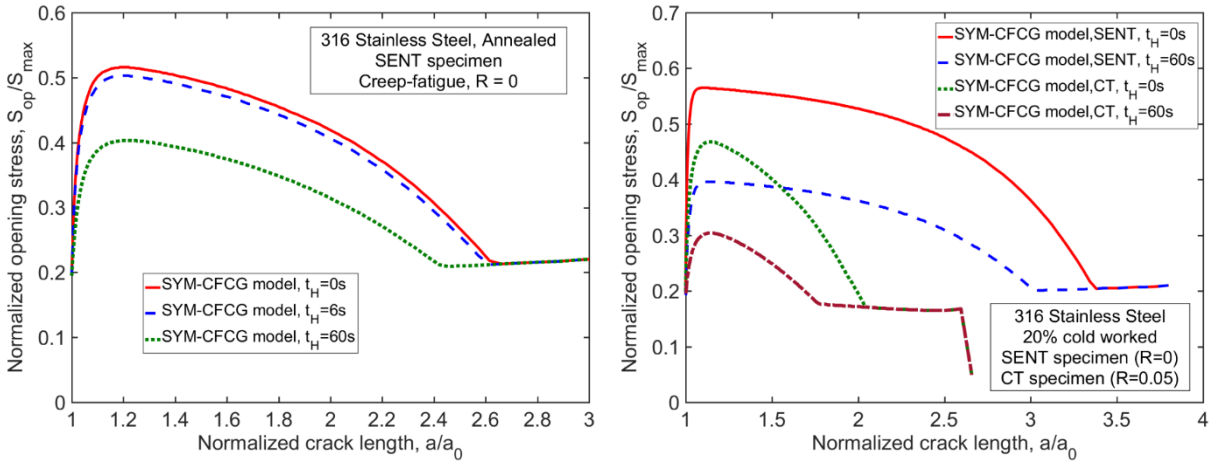

(a) **(b)**

Fig. 12. Evolution of crack-tip opening stress (SENT)/force (CT) with crack growth for fatigue and creep-fatigue loading with different hold times in AISI 316 stainless steel at 593ºC in: (a) annealed and (b) 20% cold worked conditions.

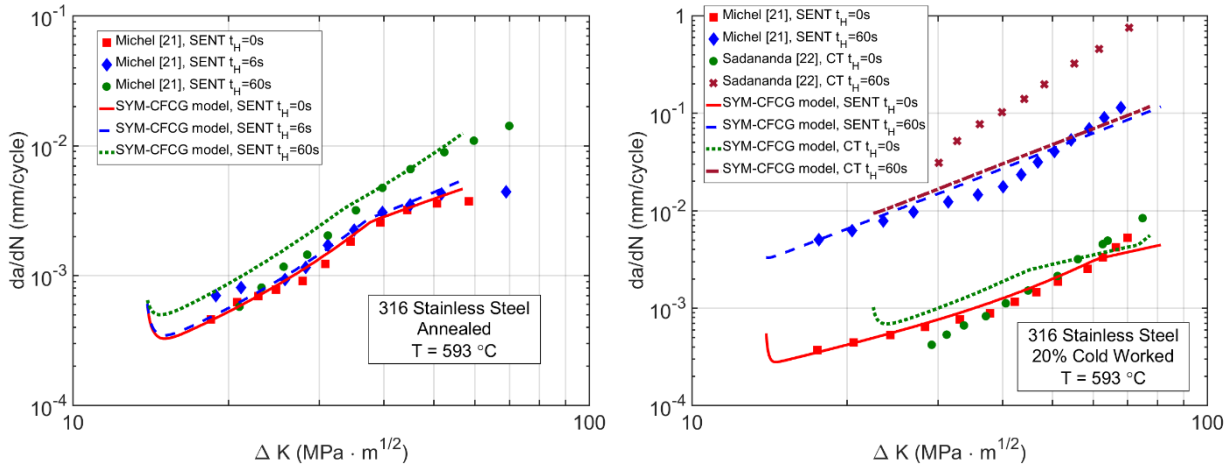

(a) **(b)**

Fig. 13. Comparison between the SYM-CFCG model predictions and experimental measurements [21-22] of creep-fatigue crack growth rates in AISI 316 stainless steel at 593ºC in: (a) annealed and (b) 20% cold worked conditions.

The SYM-CFCG model predictions of crack growth rates da/dN versus ΔK for both temperatures are shown in Fig. 13. In Fig. 13a, it can be observed that because of the small decrease in the opening stress between t_h = 0s and t_h = 6s, the difference in the crack growth rates in these two conditions is very small. However, the predicted crack growth rates for t_h = 60s increases significantly compared with the rates for the other two hold times. Fig. 13b shows the crack growth rates in the 20% cold worked SENT specimen at a load ratio of R = 0, and in the CT specimens at R = 0.05. The predictions of crack growth in SENT specimens are compared with the experimental data by Michel and Smith [21], while for the those in CT specimens the predictions are compared with the experimental data by Sadananda and Shahinian[22]. In the case of fatigue crack growth, the match between experimental and simulation data is satisfactory. In the case of creep-fatigue crack growth with t_h = 60s, the predicted values match well the Michel's experimental results, while some discrepancy is recorded with respect to Sadananda's data.

6. Conclusions

A model was proposed to study the influence of creep hold times on fatigue crack growth during creep-fatigue loading. The model was used to perform predictions of creep-fatigue crack growth in two alloys used at elevated temperatures, a nickel-based superalloy and 316 stainless steel. Several cracked geometries commonly used in fatigue and creep-fatigue crack growth testing were used for simulations. The model was numerically implemented using a strip-yield methodology, which included the effect of both plastic and creep deformations at the crack tip. In this methodology, the stress intensity factors and crack opening displacements were computed using the weight function method. It was demonstrated that enhanced creep at the crack tip and the related stress relaxation in the crack-tip plastic zone lead to increased crack opening displacements and diminished compressive stresses for the entire crack surface at minimum load in the cycle. The model results also indicate that increased creep deformation at the crack tip caused by longer hold time leads to a diminishing influence of the plasticity-induced crack closure on the crack growth, thus an acceleration of the crack growth rate during the cyclic portion of a creep-fatigue cycle. For long enough hold times, i.e., up to 3000 seconds for the studied materials, the plasticity-induced crack closure is completely overcome by the creep deformation and the added crack opening displacement induced by creep. In effect, the opening stress drops to the minimum stress in the cycle for longer hold times, which implies that the crack is fully open at minimum load. The comparison between the model predictions and experimental data is satisfactory for most of the testing conditions and materials. The model is also able to predict the loading frequency

effect and the synergistic action of creep and fatigue loading on crack growth rates. This approach provides a template for how crack growth predictions can be performed under variable creep-fatigue loading with short to moderate hold times.

Acknowledgement

The funding support for this work by the U.S. Department of Energy under the Nuclear Energy University Program (Grant DE-NE0008443) work is gratefully acknowledged.

Appendix A. Stress intensity factors and the computation of crack-tip plastic zone.

The stress intensity factor K for a cracked specimen is computed using a geometrical factor f, which is specimen dependent. Moreover, the nominal stress distribution on the crack plane is also a factor in computing K. This appendix presents formulas for K and f for several common fracture specimens. These formulas have been adapted from Wu and Carlsson [18]. They presented their equations by normalizing crack length and specimen width. In this paper, the Wu and Carlsson formulas have been modified to be used with the actual crack length and specimen width dimensions.

For a cracked specimen with a crack length a and width W subjected to a remote uniform stress S, f is calculated using the weight function method by

$$f = \int_0^{a/W} \frac{\sigma(xW)}{S} \frac{m(a/W, x/W)}{\sqrt{\pi a/W}} dx, \tag{A1}$$

where $m(a/W,x/W)$ is a weight function, and $\sigma(xW)$ is the nominal stress that would be induced at location x in the crack plane by remotely applied stress S in the un-cracked specimen. For all specimens except the CT (i.e., the MT, SENT and DENT), the remote stress produces the following nominal stress $\sigma(xW) = S$, while for the CT specimen, the nominal stress is explained below. Substituting specific formulas for $m(a/W,x/W)$ in Eq. (A1) for each specimen, one obtains the results presented below.

Formulas for K are presented for the case of a remotely applied stress S and for the case of a segment load in the crack plane $\sigma(xW) = -\sigma_0$ applied between $xW = a_0$ and $xW = a$. In order to apply these formulas to compute the size

of the crack-tip plastic zone using the Dugdale-Barenblatt model, one must replace in the *K*-formulas a_0 with a, and a with $d = a + r_{pl}$.

(a) Single-edge notched tension (SENT)

$$f = \frac{W}{\sqrt{2\pi a}} \int_0^{a/W} \frac{\sigma(xW)}{S} \sum_{i=1}^{5} \beta_i \left(\frac{a}{W}\right) \left(1 - \frac{xW}{a}\right)^{i-\frac{3}{2}} dx, \tag{A2}$$

$$K_{IS} = \frac{SW}{\sqrt{2\pi a}} \int_0^{a/W} \sum_{i=1}^{5} \beta_i \left(\frac{a}{W}\right) \left(1 - \frac{xW}{a}\right)^{i-\frac{3}{2}} dx, \tag{A3}$$

$$K_{I\sigma_0} = \frac{-\sigma_0 W}{\sqrt{2\pi a}} \int_{a_0/W}^{a/W} \sum_{i=1}^{5} \beta_i \left(\frac{a}{W}\right) \left(1 - \frac{xW}{a}\right)^{i-\frac{3}{2}} dx. \tag{A4}$$

(b) Compact-tension (CT) specimen.

$$f = \frac{1}{\sqrt{2\pi a}} \int_0^{a/W} \frac{\sigma(xW)}{S} \sum_{i=1}^{4} \beta_i \left(\frac{a}{W}\right) \left(1 - \frac{xW}{a}\right)^{i-\frac{3}{2}} dx. \tag{A5}$$

In the case of a CT specimen, the loading is applied as a concentrated force P at the pinhole, which gives a distributed stress in the crack plane as

$$\frac{\sigma(xW)}{S} = b + k\,xW, \tag{A6}$$

where $b = 4$ and $k = -6/W$. Then,

$$K_{IS} = \frac{SW}{\sqrt{2\pi a}} \int_0^{a/W} (b + kx) \sum_{i=1}^{4} \beta_i \left(\frac{a}{W}\right) \left(1 - \frac{xW}{a}\right)^{i-\frac{3}{2}} dx, \tag{A7}$$

$$K_{I\sigma_0} = \frac{-\sigma_0 W}{\sqrt{2\pi a}} \int_{a_0/W}^{a/W} \sum_{i=1}^{4} \beta_i \left(\frac{a}{W}\right) \left(1 - \frac{xW}{a}\right)^{i-\frac{3}{2}} dx. \tag{A8}$$

Appendix B. β-coefficients for the Wu-Carlson weight functions.

In this appendix, for the SENT and CT specimens, a is the crack length and W is the specimen width. For the MT and DENT specimens, a is the crack half-length, and W is the specimen half-width. The coefficients β_i used in the Appendices A, C, D and E are adapted from Wu and Carlsson [18] and are as follows.

(a) SENT specimen

$$\beta_1\left(\frac{a}{W}\right)=2.0, \tag{B1}$$

$$\beta_2\left(\frac{a}{W}\right)=\left[4\frac{a}{W}f_r'\left(\frac{a}{W}\right)+2f_r\left(\frac{a}{W}\right)+\frac{3}{2}F_2\left(\frac{a}{W}\right)\right]\Big/ f_r\left(\frac{a}{W}\right), \tag{B2}$$

$$\beta_3\left(\frac{a}{W}\right)=\left\{\frac{a}{W}F_2'\left(\frac{a}{W}\right)+\frac{1}{2}\left[5F_3\left(\frac{a}{W}\right)-F_2\left(\frac{a}{W}\right)\right]\right\}\Big/ f_r\left(\frac{a}{W}\right), \tag{B3}$$

$$\beta_4\left(\frac{a}{W}\right)=\left\{\frac{a}{W}F_3'\left(\frac{a}{W}\right)+\frac{1}{2}\left[7F_4\left(\frac{a}{W}\right)-3F_3\left(\frac{a}{W}\right)\right]\right\}\Big/ f_r\left(\frac{a}{W}\right), \tag{B4}$$

$$\beta_5\left(\frac{a}{W}\right)=\left[\frac{a}{W}F_4'\left(\frac{a}{W}\right)-\frac{5}{2}F_4\left(\frac{a}{W}\right)\right]\Big/ f_r\left(\frac{a}{W}\right), \tag{B5}$$

$$f_r\left(\frac{a}{W}\right)=\sum_{i=0}^{7}\frac{\alpha_i\left(a/W\right)^{i-1}}{\left(1-\frac{a}{W}\right)^{\frac{3}{2}}}, \tag{B6}$$

with α_0 = 1.1214, α_1 = −1.6349, α_2 = 7.3168, α_3 = −18.7746, α_4 = 31.8028, α_5 = −33.2295, α_6 = 19.1286, and α_7 = −4.6091. The functions F_i are defined as

$$F_1\left(\frac{a}{W}\right)=4f_r\left(\frac{a}{W}\right), \tag{B7}$$

$$F_2\left(\frac{a}{W}\right)=\frac{1}{12\sqrt{2}}\left[315\pi\phi\left(\frac{a}{W}\right)-105V_r\left(\frac{a}{W}\right)-208\sqrt{2}f_r\left(\frac{a}{W}\right)\right], \tag{B8}$$

$$F_3\left(\frac{a}{W}\right)=\frac{1}{30\sqrt{2}}\left[-1260\pi\phi\left(\frac{a}{W}\right)+525V_r\left(\frac{a}{W}\right)+616\sqrt{2}f_r\left(\frac{a}{W}\right)\right], \tag{B9}$$

$$F_4\left(\frac{a}{W}\right)=\sqrt{2}V_r\left(\frac{a}{W}\right)-\left[F_1\left(\frac{a}{W}\right)+F_2\left(\frac{a}{W}\right)+F_3\left(\frac{a}{W}\right)\right], \tag{B10}$$

$$\phi\left(\frac{a}{W}\right)=\frac{1}{\left(a/W\right)^2}\int_0^{a/W}s\left[f_r\left(s\right)\right]^2ds, \tag{B11}$$

$$V_r\left(\frac{a}{W}\right)=\sum_{i=0}^{7}\gamma_i\left(\frac{a}{W}\right)^i\Big/\left(1-\frac{a}{W}\right)^2, \tag{B12}$$

with $\gamma_0 = 2.9086$, $\gamma_1 = -5.5749$, $\gamma_2 = 19.572$, $\gamma_3 = -39.0199$, $\gamma_4 = 58.2697$, $\gamma_5 = -54.7124$, $\gamma_6 = 29.4039$, and $\gamma_7 = -6.8949$.

(b) CT specimen.

$$\beta_1\left(\frac{a}{W}\right) = 2.0, \tag{B13}$$

$$\beta_2\left(\frac{a}{W}\right) = \left[4\frac{a}{W} f_r'\left(\frac{a}{W}\right) + 2 f_r\left(\frac{a}{W}\right) + \frac{3}{2} F_2\left(\frac{a}{W}\right)\right] \Big/ f_r\left(\frac{a}{W}\right), \tag{B14}$$

$$\beta_3\left(\frac{a}{W}\right) = \left\{\frac{a}{W} F_2'\left(\frac{a}{W}\right) + \frac{1}{2}\left[5F_3\left(\frac{a}{W}\right) - F_2\left(\frac{a}{W}\right)\right]\right\} \Big/ f_r\left(\frac{a}{W}\right), \tag{B14}$$

$$\beta_4\left(\frac{a}{W}\right) = \left\{\frac{a}{W} F_3'\left(\frac{a}{W}\right) - \frac{3}{2} F_3\left(\frac{a}{W}\right)\right\} \Big/ f_r\left(\frac{a}{W}\right), \tag{B15}$$

$$F_2\left(\frac{a}{W}\right) = \frac{35\sqrt{2}}{12}\pi\phi\left(\frac{a}{W}\right) - 8 f_r\left(\frac{a}{W}\right), \tag{B16}$$

$$F_3\left(\frac{a}{W}\right) = \frac{28}{15} f_r\left(\frac{a}{W}\right) - \frac{7\sqrt{2}}{12}\pi\phi\left(\frac{a}{W}\right), \tag{B17}$$

$$\phi\left(\frac{a}{W}\right) = \frac{1}{(a/W)^2}\int_0^{a/W} s\left[f_r(s)\right]^2 ds, \tag{B18}$$

$$f_r\left(\frac{a}{W}\right) = \sum_{i=0}^{7}\alpha_i\left(\frac{a}{W}\right)^i \Big/ \left(1-\frac{a}{W}\right)^{3/2}. \tag{B27}$$

The coefficients in the above equation are $\alpha_0 = 1.1214$, $\alpha_1 = 0.0294$, $\alpha_2 = -2.1907$, $\alpha_3 = 3.5511$, $\alpha_4 = 6.2459$, $\alpha_5 = -21.1853$, $\alpha_6 = 20.0463$, and $\alpha_7 = -6.4967$.

Appendix C. Crack surface displacements for specimens loaded under remotely applied loading *S* (see Fig. 3b).

(a) SENT specimen

$$u(a,x,S) = \frac{SW}{E'\pi}\int_{x/W}^{a/W}\left[\sum_{i=1}^{5}\frac{\beta_i(\xi)}{2i-1}\right]\left[\sum_{i=1}^{5}\beta_i(\xi)\left(1-\frac{x}{W\xi}\right)^{i-\frac{3}{2}}\right]d\xi. \tag{C.1}$$

The factors β_i are given in Appendix B(b).

(b) CT specimen

For a CT specimen of width W and thickness B_N, loaded remotely at the pinhole by a concentrated force P, the crack surface displacements are

$$u(a,x,\sigma)=\frac{\sigma W}{E'\sqrt{2}}\int_{x/W}^{a/W} f(\xi)\sum_{i=1}^{4}\beta_i(\xi)\left(1-\frac{x}{W\xi}\right)^{i-\frac{3}{2}}d\xi\ , \tag{C.3}$$

where $\sigma = P/(WB_N)$, and

$$f(\xi)=bf_c(\xi)+kf_l(\xi), \tag{C.4}$$

with $b = 4$, $k = -6/W$ and

$$f_c(\xi)=\frac{\sqrt{2}}{\pi}\sum_{i=1}^{4}\frac{1}{2i-1}\beta_i(\xi) \tag{C.5}$$

$$f_l(\xi)=\frac{\sqrt{2}}{\pi\xi}\sum_{i=1}^{4}\frac{2}{(2i-1)(2i+1)}\beta_i(\xi) \tag{C.6}$$

The factors β_i are given in Appendix B(c).

Appendix D. Crack surface displacements for specimens loaded in the crack plane with a segment load not reaching the crack tip (see Fig. 3d).

The specimen width (or half-width) is W, crack length (or half-length) is a, and the crack surface is loaded by a segment load $\sigma(x) = \sigma$ between x_1 and x_2, where $x_1 < x_2 < a$. Then, with the notation $a_0 = \max(x_1, x)$, the crack surface displacements are as follows (adapted from Wu and Carlsson [18]).

(a) SENT Specimen

$$u(a,x,\sigma)=\frac{\sigma W}{E'\sqrt{2}}\int_{a_0/W}^{a/W} f(\xi)\sum_{i=1}^{5}\beta_i(\xi)\left(1-\frac{x}{W\xi}\right)^{i-\frac{3}{2}}d\xi\,, \tag{D.1}$$

$$f(\xi)=\frac{\sqrt{2}}{\pi}\sum_{i=1}^{5}\left\{\frac{1}{2i-1}\beta_i(\xi)\left[\left(1-\frac{x_1}{W\xi}\right)^{i-\frac{1}{2}}-\left(1-\frac{x_2}{W\xi}\right)^{i-\frac{1}{2}}\right]\right\}. \tag{D.2}$$

(b) CT specimen

$$u(a,x,\sigma)=\frac{\sigma W}{E'\sqrt{2}}\int_{a_0/W}^{a/W} f(\xi)\sum_{i=1}^{4}\beta_i(\xi)\left(1-\frac{x}{W\xi}\right)^{i-\frac{3}{2}}d\xi, \tag{D.3}$$

$$f(\xi)=\frac{\sqrt{2}}{\pi}\sum_{i=1}^{4}\left\{\frac{1}{2i-1}\beta_i(\xi)\left[\left(1-\frac{x_1}{W\xi}\right)^{i-\frac{1}{2}}-\left(1-\frac{x_2}{W\xi}\right)^{i-\frac{1}{2}}\right]\right\}. \tag{D.4}$$

Appendix E. Crack surface displacements for specimens loaded in the crack plane with a segment load reaching the crack tip (see Fig. 3c).

In this appendix, the specimen width (or half-width) is *W*, crack length (or half-length) is *a*, and the crack surface is loaded by a segment load $\sigma(x) = \sigma$ between x_1 and x_2, where $x_1 < x_2 = a$. Then, with the notation $a_0 = \max(x_1, x)$, the crack surface displacements are the following (adapted from Wu and Carlsson [18]).

(a) SENT specimen

$$u(a,x,\sigma)=\frac{\sigma W}{E'\sqrt{2}}\int_{a_0/W}^{a/W} f(\xi)\sum_{i=1}^{5}\beta_i(\xi)\left(1-\frac{x}{W\xi}\right)^{i-\frac{3}{2}}d\xi, \tag{E.1}$$

$$f(\xi)=\frac{\sqrt{2}}{\pi}\sum_{i=1}^{5}\frac{1}{2i-1}\beta_i(\xi)\left(1-\frac{x_1}{W\xi}\right)^{i-\frac{1}{2}}. \tag{E.2}$$

(b) CT specimen

$$u(a,x,\sigma)=\frac{\sigma W}{E'\sqrt{2}}\int_{a_0/W}^{a/W} f(\xi)\sum_{i=1}^{4}\beta_i(\xi)\left(1-\frac{x}{W\xi}\right)^{i-\frac{3}{2}}d\xi, \tag{E.3}$$

$$f(\xi)=\frac{\sqrt{2}}{\pi}\sum_{i=1}^{4}\frac{1}{2i-1}\beta_i(\xi)\left(1-\frac{x_1}{W\xi}\right)^{i-\frac{1}{2}}. \tag{E.4}$$

References

[1] Paris, P.C. Erdogan., F. 1963. A critical analysis of crack propagation laws. J. Basic Eng.-T ASME 85, 528-533

[2] Elber, W., 1970. Fatigue crack growth under cyclic tension. Eng. Fract. Mech. 2, 1, 37-45

[3] Sehitoglu H., Sun W., 1989. The significance of crack closure under high temperature fatigue crack growth with hold periods. Eng. Fract. Mech. 33, 3, 371-388

[4] Ramirez, J.; Potirniche, G.P., Pugesek, H., Shaber, N.; Taylor, M, Stephens, R., Charit, I., 2018, Predicting creep-fatigue crack growth rates in Alloy 709 using finite element simulations of plasticity and creep-induced crack closure, MATEC Web of Conferences, 165, 12th International Fatigue Congress, FATIGUE 2018

[5] Dugdale, D.S., 1960. Yielding of steel sheets containing slits. J. Mech. Phys. Solids 8, 2, 100-104

[6] Barenblatt, G.I., 1962. The mathematical theory of equilibrium cracks in brittle fracture. Adv. Appl. Mech. 7, 55–129

[7] Newman Jr., J.C., 1981. A crack-closure model for predicting fatigue crack growth under aircraft spectrum loading, in "Methods and models for predicting fatigue crack growth under random loading, ASTM STP 748, J.B. Chang and C.M. Hudson (Eds.), American Society for Testing and Materials, 53-84

[8] deKoning AU, Liefting G. 1988. Analysis of crack opening behavior by application of a discretized strip yield model, ASTM STP 982, 437—58

[9] Wang, G.S., Blom, A.F., 1991. Strip model for fatigue crack growth predictions under general load conditions. Eng. Fract. Mech. 40, 3, 507-533

[10] Daniewicz, S.R., Collins, J.A., Houser, D.R., 1994. Elastic-plastic analytical model for predicting fatigue crack growth in arbitrary edge-cracked two-dimensional geometries with residual stress. Int. J. Fatigue 16, 2, 123-133

[11] Kim, J.H., Lee, S.B., 2000. Fatigue crack opening stress based on the strip-yield model. Theor. Appl. Fract. Mec. 34, 1, 73-84

[12] Fischer, C., Schweizer, C., Seifert, T., 2015 Assessment of fatigue crack closure under in-phase and out-of-phase thermomechanical fatigue loading using a temperature dependent strip yield model. Int. J. Fatigue 78, 22-30

[13] Potirniche, G.P., 2012. A numerical strip-yield model for the creep crack incubation in steels, ASTM STP 1546, 197-214

[14] Piard, A., Gamby, D., Carbou, C., Mendez, J., 2004. A numerical simulation of creep-fatigue crack growth in nickel-base superalloys. Eng. Fract. Mech. 71, 2299-2317

[15] Riedel, H., Rice, J.R., 1980. Tensile crack in creeping solids, *Fracture Mechanics: Twelfth Conference, ASTM STP 700*, American Society for Testing and Materials, 112-130

[16] Hutchinson, J.W., 1968. Singular behavior at the end of a tensile crack in a hardening material, J. Mech. Phys. Solids, 16, 13-31

[17] Riedel, H., 2000. Fracture at high temperatures, Springer-Verlag, Heidelberg

[18] Wu, X.-R., Carlsson, A. J., 1991. Weight functions and stress intensity factor solutions, Pergamon Press, Oxford, UK

[19] McClung, R.C., 1994. Finite element analysis of specimen geometry effects on fatigue crack closure, Fatigue and Fracture Engineering Materials and Structures, 17(8), 861-872

[20] Newman Jr, JC. Advances in finite element modeling of fatigue crack growth and fracture. Fatigue 02: The Eight International Fatigue Congress Stockholm, Sweden, 2–7 June 2002

[21] Michel, D.J., Smith, H.H., 1976. Effect of hold time on elevated temperature fatigue crack propagation in types 304 and 316 stainless steel. ASME (MPC-3), 391-415

[22] Sadananda, K., Shahinian, P. 1980. Effect of environment on crack growth behavior in austenitic stainless steels under creep and fatigue conditions. Metall. Trans. A 11, 267-276

[23] British Stainless Steel Association, Elevated temperature physical properties of stainless steels, https://www.bssa.org.uk (accessed 13 March 2018)

[24] American Iron and Steel Institute, High-temperature characteristics of stainless steels, A designers' handbook series, No. 9004, https://www.nickelinstitute.org/~/Media/Files/TechnicalLiterature/High_TemperatureCharacteristicsofStainlessSteel_9004_.pdf (accessed 26 March 2018)

[25] AKSteel, 316/316L stainless steel, product data bulletin, https://www.aksteel.com/sites/default/files/2018-01/316316L201706_2.pdf (accessed 14 April 2018)

[26] Monteiro, S.N., da Luz, F.S., Pinheiro, W. A., Brandao, L. P. M., de Oliveira Braga, F., de Assis, F. S., 2017. Creep parameters and dislocation structure in AISI 316 Austenitic Stainless Steel from 600°C to 800°C. Materials Research, 20, 231-235, DOI: http://dx.doi.org/10.1590/1980-5373-MR-2016-0998

Highlights

- Hold time during creep-fatigue loading decreases plasticity-induced crack closure
- Hold time increases crack surface displacements and reduces crack opening stresses
- Longer creep hold times lead to faster crack growth rates during cyclic loading
- Hold time effect on crack closure highlights the interaction of creep and fatigue